

Blur remediation in NEAR MSI images

D. R Golish¹, D. N. DellaGiustina¹, K. J. Becker¹, C. A. Bennett¹, and M. K. Crombie²

¹Lunar and Planetary Laboratory, University of Arizona, Tucson, AZ, USA

²Indigo Information Services, LLC

Corresponding author:

Dathon R Golish (dgolish@orex.lpl.arizona.edu)

1415 N. 6th Ave. Tucson, AZ 85705

Keywords: Eros, Asteroids, Image processing

Abstract

Due to contamination on the outer optic of the NEAR-Shoemaker Multispectral Imager (MSI), all surface-resolved images of Eros acquired by MSI had wavelength-dependent degradation. The MSI team designed and implemented a preliminary correction for the blur during mission operations and archived the results with the original camera data. While extremely successful, the preliminary correction was less effective for the 450 and 1100 nm passbands. Here we implement a new correction, based on the MSI team's original process, to improve the blur remediation for all MSI filters, particularly those at the extreme wavelengths. The new method improves the effective resolution of the deblurred images over the preliminary remediation for all filters. Moreover, for all filters, our method preserves the 21-39% of the pixels that were lost (or obscured by artifacts) with the preliminary remediation. We apply the new method to the complete MSI dataset of resolved Eros images and archive the results for future scientific use.

1 INTRODUCTION

The Near Earth Asteroid Rendezvous – Shoemaker (NEAR; Cheng et al., 1997) spacecraft orbited and studied the surface of asteroid (433) Eros for a year from 14 February 2000 to 12 February 2001. Eros is a near-Earth S-type asteroid (Murchie, 1996) approximately 34 km long with an 11×11 km cross-section (Zuber et al., 2000). NEAR was the first mission to observe an asteroid from orbit and provided a broad dataset characterizing Eros's surface in unprecedented detail. Unfortunately, prior to these observations, during a failed orbit insertion maneuver on 20 December 1998, the NEAR thrusters expelled >28 kg of hydrazine fuel on to the spacecraft. Some fraction of this volume was deposited on to the outer optical surface of the NEAR Multispectral Imager (MSI; Hawkins, 1998; Murchie et al., 1999, 2002b), causing spectrally-dependent blurring for all of MSI's filters. The MSI camera was a five-element refractive telescope with eight filter positions. Seven narrowband filters covered wavelengths from 450

36 to 1050 nm, while one panchromatic filter covered from 600 to 800 nm. The blurring was worst at the
37 shortest (450 nm) and longest (1050 nm) wavelengths. Because this contamination occurred before any
38 surface-resolved imaging of Eros, the entirety of the resolved data set was degraded.

39 The MSI team took extensive observations of Canopus, the second brightest star in the sky, to
40 characterize the point spread function (PSF) of the optics after contamination. These observations
41 imaged Canopus in different regions of the detector and with all eight filters. Li et al. (2002) used a
42 subset of these observations to develop a preliminary remediation and the NEAR team supplied those
43 deblurred images to the Small Bodies Node (SBN) at the Planetary Data System (PDS).

44 Li et al. (2002) estimated a radially symmetric PSF for each MSI filter to deblur the images with a Fast
45 Fourier Transform (FFT) based method. This method recovered much of the spatial resolution for the
46 central wavelengths (550 – 1000 nm), though the extreme wavelengths were less successful (450, 1050
47 nm). In addition, limitations in the size of the FFT window led to cropping the image in one direction and
48 strong artifacts on the edges of the images. The effective usable area of the restored images was
49 therefore reduced (Li et al., 2002), however this shortcoming was mitigated by a targeting strategy that
50 included extra overlap between images to ensure no coverage was lost. Nonetheless, the procedure
51 enabled all of NEAR’s surface analysis and subsequent science. These analyses included global mapping
52 (Buczkowski et al., 2008; Bussey et al., 2002; Veverka et al., 2000), color mapping (Murchie et al., 2002a;
53 Riner et al., 2008), shape model and topographic analysis (Buczkowski et al., 2008; Thomas et al., 2002),
54 geology (Cheng et al., 2002; Dombard et al., 2010; Izenberg et al., 2003; Robinson et al., 2002; Thomas
55 and Robinson, 2005), and photometric modeling (Li et al., 2004).

56 We have the opportunity now, 20 years after MSI observed the surface of Eros, to improve upon this
57 preliminary remediation in a number of ways. Increased computational resources allow us to deviate
58 from efficiency-based design choices such as FFT windows that are powers of two, eliminating cropping
59 and edge artifacts. Moreover, we can take advantage of the full set of Canopus images to develop a
60 more advanced PSF model for each filter, including breaking the assumption of radial symmetry. The
61 extent of the Canopus dataset suggested we might explore the feasibility of PSF that varies across MSI’s
62 field of view, though that proved not to be viable. In this manuscript, we detail the advanced modeling
63 and deblurring process that we applied to the entire MSI orbital dataset.

64 2 MSI PSF

65 2.1 Deblurring algorithm

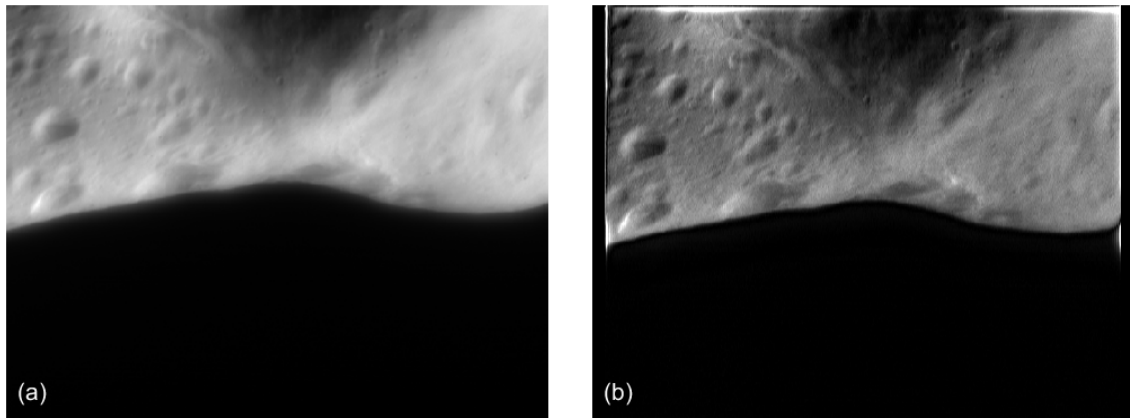
66 Our deblurring methodology is derived from the method used in the preliminary MSI remediation (Li et
67 al., 2002). In both works, the degraded image, $g(x,y)$, is expressed as the convolution of the original
68 signal, $f(x,y)$, and a distorting function, $h(x,y)$, with some additive noise, k .

69
$$g(x,y) = f(x,y) * h(x,y) + k \quad (1)$$

70 If we assume we can model or estimate the distorting (blurring) function and noise level, we can utilize a
71 Wiener deconvolution to restore the original image (Dhawan et al., 1985). Wiener deconvolution is a
72 common restoration method in which we transform the components to Fourier space with an FFT,
73 invert the blurring function, and transform back to physical space to restore the original image. In this
74 work, we used a built-in MATLAB function, *deconvwnr*, to perform the Wiener deconvolution. To
75 evaluate the efficacy of the MATLAB function, we re-implemented the preliminary MSI remediation in

76 MATLAB without *deconvwnr*. We verified that the MATLAB implementation produced identical results to
77 the original MSI remediation. We then compared the results of the *deconvwnr* algorithm with the re-
78 implementation of the preliminary MSI remediation method and found that the former had qualitatively
79 improved noise reduction (evaluated by visual inspection).

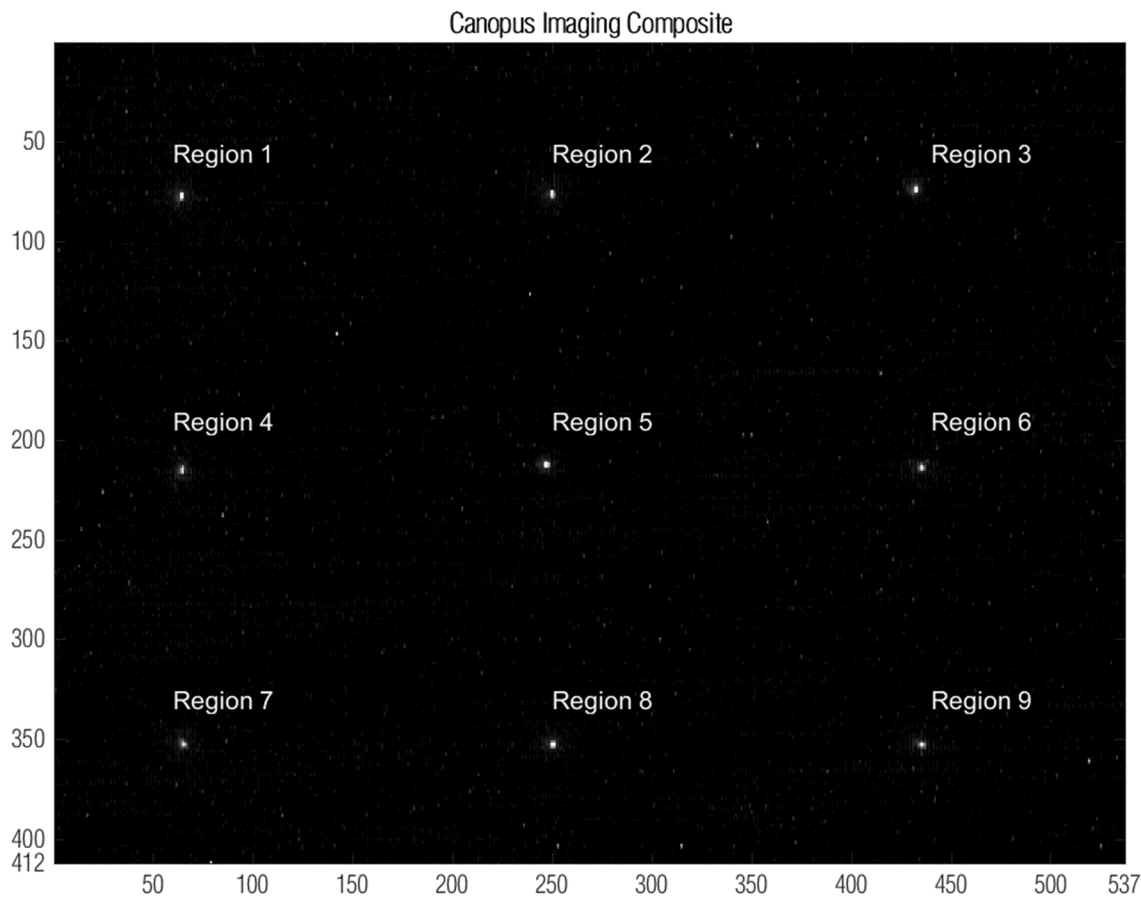
80 The mathematical basis for our new method is otherwise similar, with one important difference. The
81 preliminary remediation cropped the degraded images to 412×512 (from 412×537). While this was
82 necessary for their implementation, it removed 25 lines (columns) from the images. Moreover, the
83 discontinuous boundaries at the edges of the images caused FFT ringing (Figure 1(b)). Li et al. (2002)
84 estimated that the usable pixel area of their remediated images was reduced to ~21% for
85 monochromatic analyses and ~39% for color analyses. To avoid this loss, we make two changes. First, we
86 remove the requirement that we perform FFT operations with powers of two (e.g., 512×512), so we do
87 not have to crop the image. Secondly, we apply a tapered symmetric padding to all edges of the images.
88 That is, we expand the image by an arbitrary amount (e.g., 50 pixels) in each direction and reflect the
89 image data across the boundary. We then taper the data in the padded region such that the signal
90 approaches 0 at the new edges of the image (Figure 1(c)). This forces the image to be approximately
91 zero at all boundaries and FFT artifacts that result from edge discontinuities are eliminated. Even
92 without improved remediation (Section 3), these changes alone restore the lost pixels, increasing the
93 usable areas by 21-39%.



95 Figure 1: Correcting a degraded image (*m0128004492*, acquired at 09:31:06 on 2000 March 09, 14 km wide)
 96 with its original aspect ratio (a) will produce FFT artifacts at the edges (b). Applying a tapered symmetric padding (c)
 97 across this boundary (dashed orange line) eliminates the artifacts.

98 2.2 Point Source Data

To apply the remediation algorithm, we must estimate the distorting function (i.e., the system PSF after hydrazine decontamination, $h(x,y)$ in Eqn. 1). After the hydrazine contamination event, MSI collected >7,000 images of Canopus in all eight filters and in several regions of the detector. MSI acquired the Canopus images throughout 1999, 2000, and 2001, however the MSI team saw no evidence of temporal changes in the MSI PSF (Li et al., 2002) and our analysis confirmed this. The MSI team designed the Canopus observations such that Canopus fell in one of nine regions (in a 3x3 grid) of the detector. With the exception of the extreme wavelengths (450 and 1100 nm) and the panchromatic filter, MSI imaged Canopus in all nine regions for the five remaining filters. For those underrepresented filters, MSI imaged Canopus in regions 3, 5, and 8 (Figure 2). However, the majority of images for all filters were in the central region, even those with full coverage acquired as few as 16 images in each region, as shown in Table 1.



111 Figure 2: Composite of nine Canopus images with filter 4 (900 nm) in the nine detector regions.

112

113

114

115

116 *Table 1: Region layout and number of images of Canopus acquired by MSI per region and filter acquired*

Filter 1 (550 nm)		
16	16	32
16	667	16
16	94	16

Filter 2 (450 nm)		
0	0	16
0	642	0
0	88	0

Filter 3 (760 nm)		
16	12	32
16	659	16
16	107	16

Filter 4 (950 nm)		
16	16	32
16	804	16
16	93	16

Filter 5 (900 nm)		
16	16	32
16	599	16
16	65	16

Filter 6 (1000 nm)		
16	16	32
16	549	16
16	96	16

Filter 7 (1050 nm)		
0	0	16
0	1376	0
0	173	0

Filter 0 (pan)		
0	0	16
0	532	0
0	43	0

117

118 2.3 Aspect Correction

119 All Canopus images are available on the PDS SBN in the Eros MSI Cruise and Orbit bundles. The MSI team
120 archived all MSI images in Flexible Image Transport System (FITS) format, with associated label files (per
121 image) containing additional metadata. This work, for both PSF modeling and deblurring, uses the Level
122 2 calibrated MSI data archived with the SBN. Level 2 images are calibrated for bias signal, dark current,
123 charge smear, responsive non-uniformity, and radiometric conversion (Murchie et al., 2002b, 1999).

124 The images were archived in their native pixel format – 244 rows by 537 columns, where the pixels are
125 $27 \times 16 \mu\text{m}$. All data processed in this work and displayed in this manuscript have been aspect-corrected
126 to 412×537 to accommodate the rectangular pixels. The resized images represent a physically
127 meaningful aspect ratio. While we did explore modeling and correcting the image degradation in the
128 native pixel space, as proposed by Li et al. (2002), we found that it did not fundamentally improve the
129 remediation.

130 Our remediation, therefore, inherently included resizing the image. We resized the images with
131 MATLAB’s *imresize* function and a bicubic interpolator, though other interpolators (or resizing as part of
132 the Fourier space remediation) are equally valid. Rather than embed another resizing process into the
133 data, we elected not to compress the images back to their native pixel format after remediation. Any
134 subsequent scientific analyses using MSI data will undoubtedly occur with aspect-corrected images.
135 While this necessarily requires ~40% more storage space for the data, it avoids burdening the data with
136 an additional noisy step that will be immediately reversed by any future users.

137 2.4 Reducing Data

138 Unfortunately, modeling of the MSI PSF is challenging owing to the presence of *aliasing* on the detector.
139 The MSI detector was a frame transfer charge coupled device (CCD). Like many such devices (Golish et

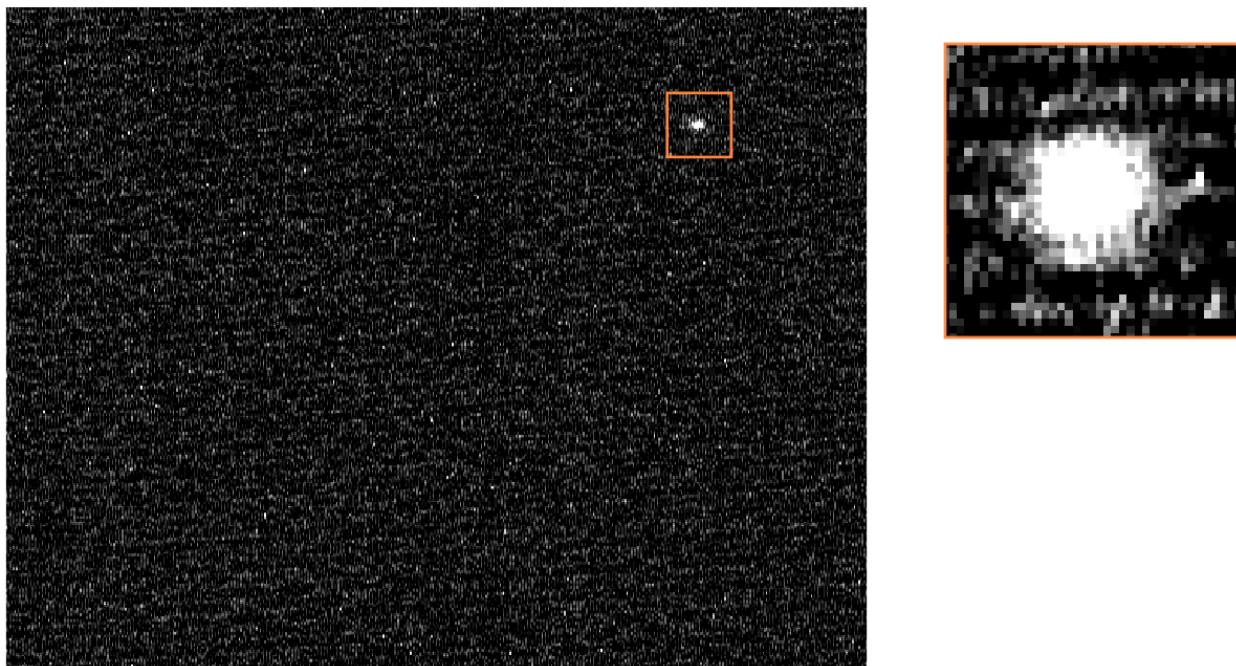
140 al., 2020; Sierks et al., 2011), the MSI pixels do not have 100% fill factor (Murchie et al., 1999). Anti-
141 blooming channels between pairs of pixel columns obscured 8 μm bands (4 μm from each column) in an
142 asymmetric pattern. An additional \sim 6.5 μm at the bottom of each pixel were not sensitive to light. As a
143 result, the effective fill factor of the pixels was 0.5675, with aliasing in both the row and column
144 directions. For an extended source, the insensitive regions blocked \sim 44% of the incoming light, but was
145 accommodated by the radiometric calibration of the camera (Murchie et al., 2002b, 1999). However,
146 when observing a point source, and with a PSF width on the order of a pixel, the fraction of the incoming
147 light that was detected depended strongly on where the point source was imaged relative to the pixel
148 grid.

149 Without exact point source locations, and a precise measure of the pixel geometry, automatic correction
150 of the Canopus images is impossible. Instead, we coadded many images of Canopus such that we
151 successfully sampled the peak of the PSF, while also increasing the signal to noise ratio (SNR) in the
152 distal parts of the PSF, which are broad and dim.

153 To reliably combine 10s (or 100s) of point source images, we first had to center the images of Canopus
154 for each filter/region combination. The pointing for every MSI image is described by the SPICE kernels
155 archived by the Navigation and Ancillary Information Facility (NAIF; Acton et al., 2018). The SPICE toolkit
156 allows us to calculate the right ascension and declination (RA/dec) for the four corners of a given image.
157 We then transformed the nominal RA/dec (95.988° / -52.696°) of Canopus into an approximate pixel
158 location for Canopus in the image. We cropped the image to an $N \times N$ window around the nominal
159 Canopus location. The size of N depended on the filter, due to variation in the PSF width as a function of
160 wavelength – 40 pixels for filters 0, 1, 2, and 3; 20 pixels for filter 5, 16 pixels for filters 4 and 6; and 10
161 pixels for filter 7. We calculated the weighted centroid of the resulting crop to identify the center of the
162 image of Canopus. This method, which is highly sensitive to the broad, shallow wings of the PSF,
163 consistently aligned the images. Optimizing the crop window was critical for this method. Too large a
164 window allowed background noise and/or cosmic rays to perturb the weighted centroid. Alternatively,
165 too small a window excluded the wings of the PSF and reduced the centroid fidelity.

166 For each filter/region combination, we then combined all available images of Canopus into a single
167 image via a median operation. Because of aliasing on the detector, the central peak of a point source
168 image could be masked by as much as 80% (Murchie et al., 1999). This had a negligible effect on the
169 wings of the PSF – it consistently masked \sim 44% of the light, but was not dependent on the location of
170 the PSF with respect to the pixel grid. The original remediation mitigated this effect by constructing a
171 composite PSF from four concentric zones (Li et al., 2002). We mimic and simplify this mitigation by
172 representing the PSF as the composite of two regions when combining Canopus images. For the central
173 3x3 pixel region surrounding the peak of the PSF, we included only the brightest images. This effectively
174 assumed that for many locations of Canopus, with respect to the pixel grid, some fraction would be
175 centered on the light-sensitive region. Setting this threshold too high would allow too many images
176 where the PSF was not well centered. Setting it too low would reduce the SNR we gain by combining
177 multiple images. We found that a threshold of 5% achieved an optimal balance between these two
178 factors. However, for the underrepresented filter/region combinations, 5% of 16-32 images is only 1-2
179 images, which do not produce a meaningful median. Therefore, for those underrepresented regions, we
180 also implemented a minimum, where at least three images must be included in every median. Again,
181 this was a balance between too few and too many images. Clearly, the limited number of Canopus
182 images outside of the central detector region reduced the statistical strength of this method.

183 Finally, we note that some MSI images had residual background noise (Figure 3). We expect that this
184 noise, based on its sinusoidal structure, is likely uncorrected read noise from the detector electronics
185 (Janesick, 2001). Moreover, the noise pattern is not eliminated by the median combination of several
186 images, indicating that it is a somewhat fixed pattern in the detector readout. The level of the noise is
187 sufficiently low (<4% of the peak signal) that it has negligible impact on any radiometric or
188 morphological use of the images. However, for blur remediation, which includes modeling the wings of
189 the PSF, a sinusoidal background can significantly perturb the model. Modeling of the noise proved
190 ineffective – as likely to introduce artifacts as it was to remove the sinusoidal noise. Presumably, this
191 noise source is best removed during image calibration. However, rather than attempt to recreate the
192 MSI calibration pipeline, we instead simply set all negative pixel values in the co-added image to zero.
193 This removed the majority of the sinusoidal pattern, but has no significant effect on our measurement of
194 the PSF, which necessarily includes only positive values.



195
196 *Figure 3: Sinusoidal background noise in the images can perturb the PSF model. Setting all negative pixel values to 0 removes*
197 *the sinusoidal noise without significantly affecting the PSF measurement.*

198 2.5 PSF Model

199 The original remediation represented the MSI PSF as a radially symmetric distribution, created by taking
200 the median of many images of Canopus (utilizing the composite structure described in Section 2.4) and
201 averaging the result in the radial dimension to increase the SNR (Li et al., 2002). In contrast, we modeled
202 the MSI PSF functionally and not as the direct reduction of image data. The data averaging method used
203 by Li et al. (2002) has the advantage that it can represent small variations in the PSF which a functional
204 model is less likely to capture. This is particularly relevant for a PSF model, which is classically
205 represented as a sinc function, which includes non-monotonic behavior in its wings. However, that
206 representation is prone to variation due to noise. On the other hand, a functional representation has the
207 advantage that it forces (with the appropriate functional form) physically realistic conditions (e.g., the
208 PSF must always be positive). It is also more flexible, because we are able to create and adjust a PSF

209 image (used in the deblurring process, Section 2.1) for any size array – as opposed to the data averaging
 210 method, which creates a fixed PSF image of a fixed size. This flexibility (particularly the ability to adjust
 211 the PSF on the fly) will be important for optimizing the PSF (Section 2.7).

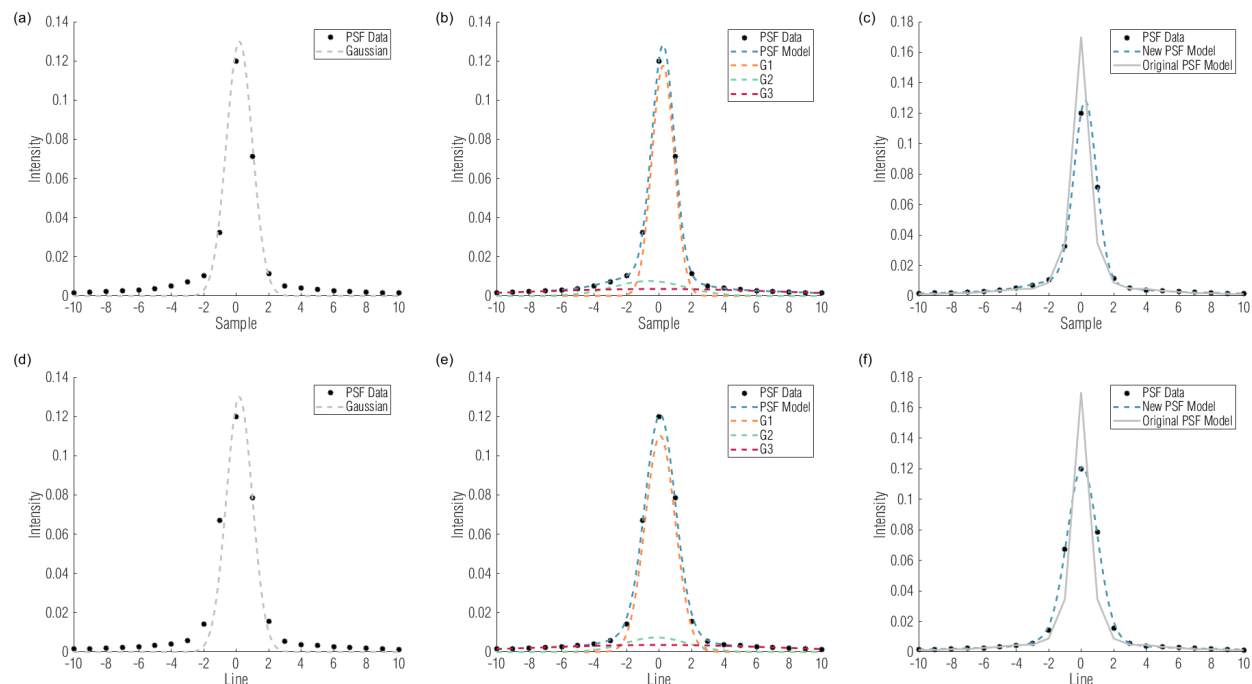
212 The MSI PSF is characterized by a central peak, which broadened due to the contamination (Li et al.,
 213 2002), a relatively high shoulder, and broad shallow wings (Figure 4(a,d)). While the ideal representation
 214 of a PSF is a sinc function, the broad, shallow shoulder and wings cause a physically-motivated form to
 215 be insufficient. Instead, we chose to utilize an empirical form of the sum of three Gaussians. While
 216 clearly an approximation, the Gaussians allow us to capture the three components of the PSF (peak,
 217 shoulder, and wings) separately (Figure 4(b,e)). Moreover, the PSF is somewhat asymmetric; the three
 218 Gaussian form allows us to model the x (sample) and y (line) directions. The three Gaussian model has
 219 the form

$$220 I_{PSF} = C_1 e^{-(x-x_1)^2/\sigma_{x1}^2 + (y-y_1)^2/\sigma_{y1}^2} + C_2 e^{-(x-x_2)^2/\sigma_{x2}^2 + (y-y_2)^2/\sigma_{y2}^2} + C_3 e^{-(x-x_3)^2/\sigma_{x3}^2 + (y-y_3)^2/\sigma_{y3}^2}$$

221 (2)

222 where C_n is the peak value, σ_{xn} and σ_{yn} are the widths, and x_n and y_n are the center offsets, in the x
 223 (sample) and y (line) directions. We model the PSFs in MATLAB with the curve fitting toolbox (*fit*), using
 224 a non-linear least squares solver. The solver optimized the free parameters to minimize the difference
 225 between the measured data and the model. After fitting, the model is normalized and centered such
 226 that the peak of the model is equal to 1 and located at 0,0.

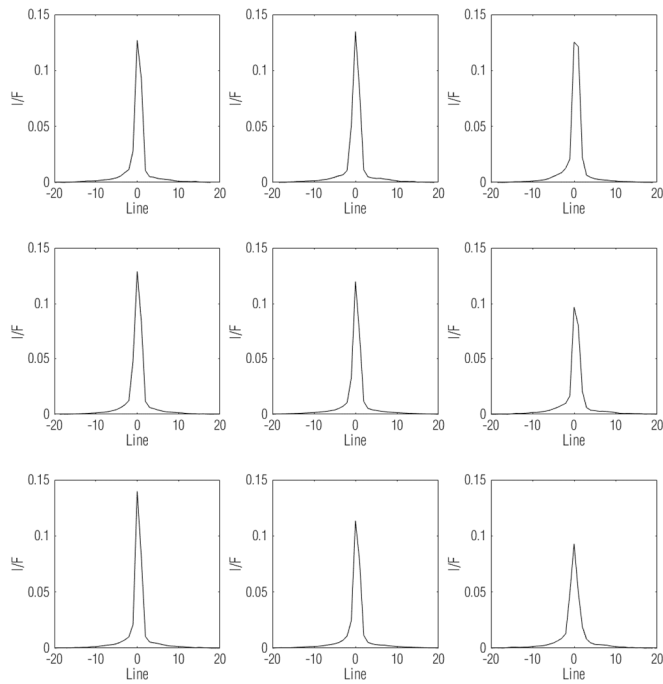
227 When compared with the PSF designed for the original remediation of 950 nm images (Figure 4(c,f)), the
 228 new remediation has a broader PSF, relative to its peak. The original remediation used the brightest
 229 pixel in any Canopus image to define the brightness of the central pixel of the PSF. This will inherently be
 230 larger than our method, which takes the median of the brightest 5% of the images for the central 3x3
 231 pixel region. The PSF models for the original remediation were archived (and applied) as 512x512 FITS
 232 images. Correspondingly, there is some visible quantization in the original PSF model.



234 Figure 4: Modeling the 950 nm MSI PSF in the x/sample (a,b,c) and y/line(d,e,f) directions with a single Gaussian does not
235 capture its width (a,d). Modeling it as the sum of three Gaussians captures the central peak, shoulder and wings (b,d).
236 Compared with the PSF from the original remediation (c,f), we see a somewhat broader PSFs relative to its peak.

237 2.6 Spatial Variance

238 With more images in use than with the original remediation, we investigated whether a spatially variant
239 PSF might improve the deblurring results. We repeated the analysis described above and produced PSF
240 models for every region that has Canopus data. Unfortunately, the sparsity of data in the outer regions
241 of the detector (Table 1) resulted in significant variation between the regions. Figure 5 shows cross-
242 sections of the coadded Canopus images described in Section 2.4 for filter 4 (950 nm). Even for filter 4,
243 which has the most post-contamination Canopus data, the peak value of the PSF varies by ~15%
244 between regions. While the variation might be indicative of a spatially variant optical sensitivity, this is
245 both physically unlikely (the contamination is on the outer surface of the lens only, not near any optical
246 pupil) and unsupported by the data. All filters with Canopus data in more than three regions have
247 region-to-region variability >12%. Filters 2, 7, and 0 only have Canopus imaging in three regions, making
248 any spatial variation impossible to detect. Instead, we suspect that aliasing, which reduces the fidelity of
249 the PSF measurement, results in significant variation between the regions, some of which have only 16
250 or 32 measurements per filter (Table 1). Nonetheless, we did attempt to apply the PSFs modeled in the
251 outer regions to evaluate their efficacy. In every case, a regional PSF recovered less image quality than
252 the PSF designed from the center region, even in the area for which the regional PSF was designed. We
253 conclude that there is not enough Canopus imaging in the exterior regions to support accurate PSF
254 modeling, and by extension, a spatially variant correction. We elect to use only image data from the
255 central region of each filter to model each per-filter PSF.



256

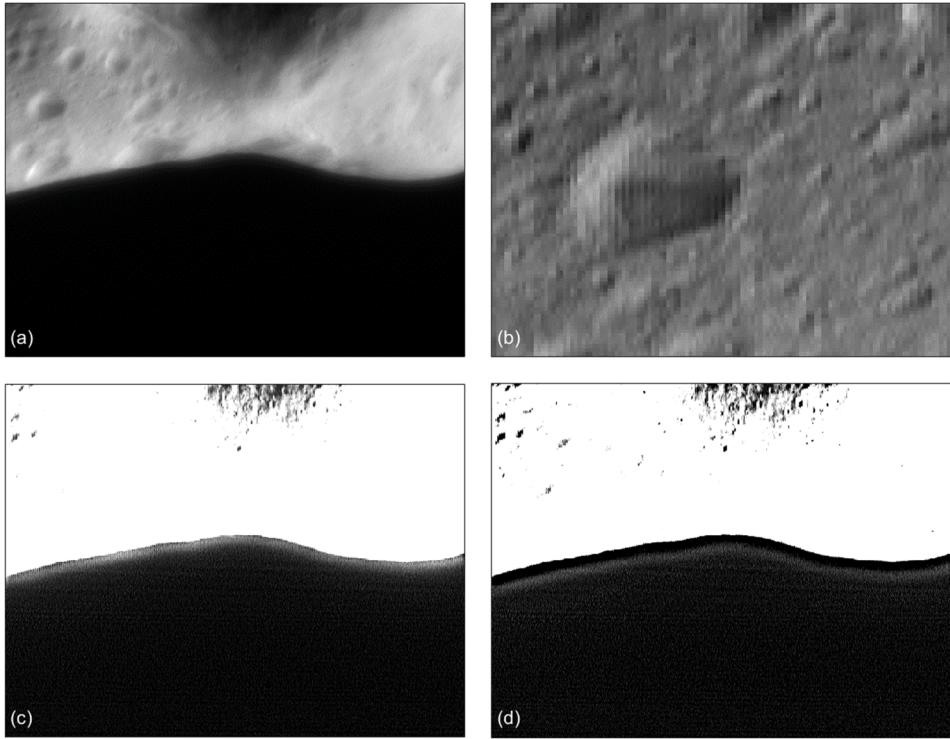
257 Figure 5: Cross-sections of coadded measurements of Canopus imaged with filter 4 (950 nm), shows significant variation
258 between detector regions. Region layout matches that shown in Figure 2.

259 2.7 Manual PSF adjustment

260 Our initial application of the PSF models to deblur the image produced unsatisfactory results. Though
261 the new PSFs recovered somewhat more information than the original remediation, they had a number
262 of issues. Fortunately, the initial models were close and our functional modeling strategy allowed us to
263 adjust the PSF and rerun the deblurring algorithm (Section 2.1) to mitigate these issues. We performed
264 this process iteratively to optimize the PSFs.

265 The width of the central Gaussian in the PSF model was has the strongest influence on the amount of
266 deblurring achieved. However, when deburring the original image (Figure 6(a)) with the automatically
267 derived PSF model, the remediated images had columnar pixelization (Figure 6(b)). These artifacts are
268 likely a result of the Fourier-based deblurring method (Section 2.1) and the high degree of aliasing on
269 the MSI detector (Murchie et al., 1999). As discussed in Section 2.4, we selected a subset of Canopus
270 images to model the central 3x3 region of the PSF to mitigate the impact of aliasing masking the true
271 brightness of a point source. However, to the extent that this mitigation is imperfect, the PSF model for
272 the central Gaussian will be less accurate. We found that narrowing the width of the central Gaussian in
273 the y (line) direction helped reduce ringing around high contrast boundaries. Moreover, the MSI
274 detector is asymmetrically aliased in x direction. Correspondingly, we found that increasing the width of
275 the central Gaussian in the x (sample) direction reduced the columnar artifacts.

276 In practice, we found that the automatic model identified the width of the Gaussian representing the
277 shoulder accurately. Small changes (~20%) in this width had little impact on the resulting deblurred
278 images. However, our measurements of the wings of the models were noisy; the signal level in the wings
279 is low and aliasing reduced the efficacy of the image coadding. The width of the Gaussian representing
280 the wings controlled the extent to which the light spread, creating a ‘glow’ (Figure 6(c)) or ‘halo’ (Figure
281 6(d)) at transitions between a bright and dark area of the scene, e.g., the limb of the asteroid. As the
282 width of the broadest Gaussian decreased, the glow on the limb increased. As the width increased, the
283 halo surrounding the asteroid increased. We adjusted the width of the Gaussian to minimize the
284 intensity of both effects, though the choice was inherently a trade-off between them.



285

286 *Figure 6: Recovering a contaminated MSI image (m012800492, a) with the automatically derived PSF model produced artifacts,*
 287 *including columnar noise (b), glow at high contrast boundaries (c), and halos at high contrast boundaries (d).*

288 2.8 Determination of noise term

289 In the absence of noise, the ideal PSF would perfectly correct the degraded images. In practice, a variety
 290 of noise sources (e.g., read noise, shot noise, fixed pattern noise, stray light; (Janesick, 2001; Murchie et
 291 al., 2002b, 1999) and an imperfect PSF model inhibit the correction by amplifying the noise. The noise
 292 term in a Wiener deconvolution (k in Eqn. 1) mitigates this effect by attenuating frequencies with low
 293 SNR. Practically, we must increase the noise term for images with lower SNR or when their PSF model is
 294 less accurate. Like Li et al. (2002), we find that a derived or automatically defined noise term does not
 295 perform well, so we define it by manually adjusting it to produce the best remediation. However, the
 296 noise term and PSF model are directly related. As such, determining the noise term is inherently a trade-
 297 off between improving image sharpness and amplifying noise and FFT artifacts.

298 We iteratively modified both the PSF shape and noise term to produce the best visual results.
 299 Unfortunately, we were not able to develop an automatic method of determining image quality. The
 300 artifacts introduced by over-processing the images have the same characteristics (e.g. high frequency
 301 content, high contrast, gradient steepness) that are typically used as image quality metrics. Therefore,
 302 we manually optimized the Gaussian width and noise terms to produce the best visual results (Table 2).

303 *Table 2: PSF model parameters for each MSI filter*

<i>Filter</i> <i>(wavelength, nm)</i>	1 (550)	2 (450)	3 (760)	4 (950)	5 (900)	6 (1000)	7 (1050)	0 <i>(pan)</i>
C_1	0.85	0.66	0.88	0.92	0.92	0.91	0.81	0.89
C_2	0.086	0.21	0.084	0.059	0.056	0.069	0.18	0.065

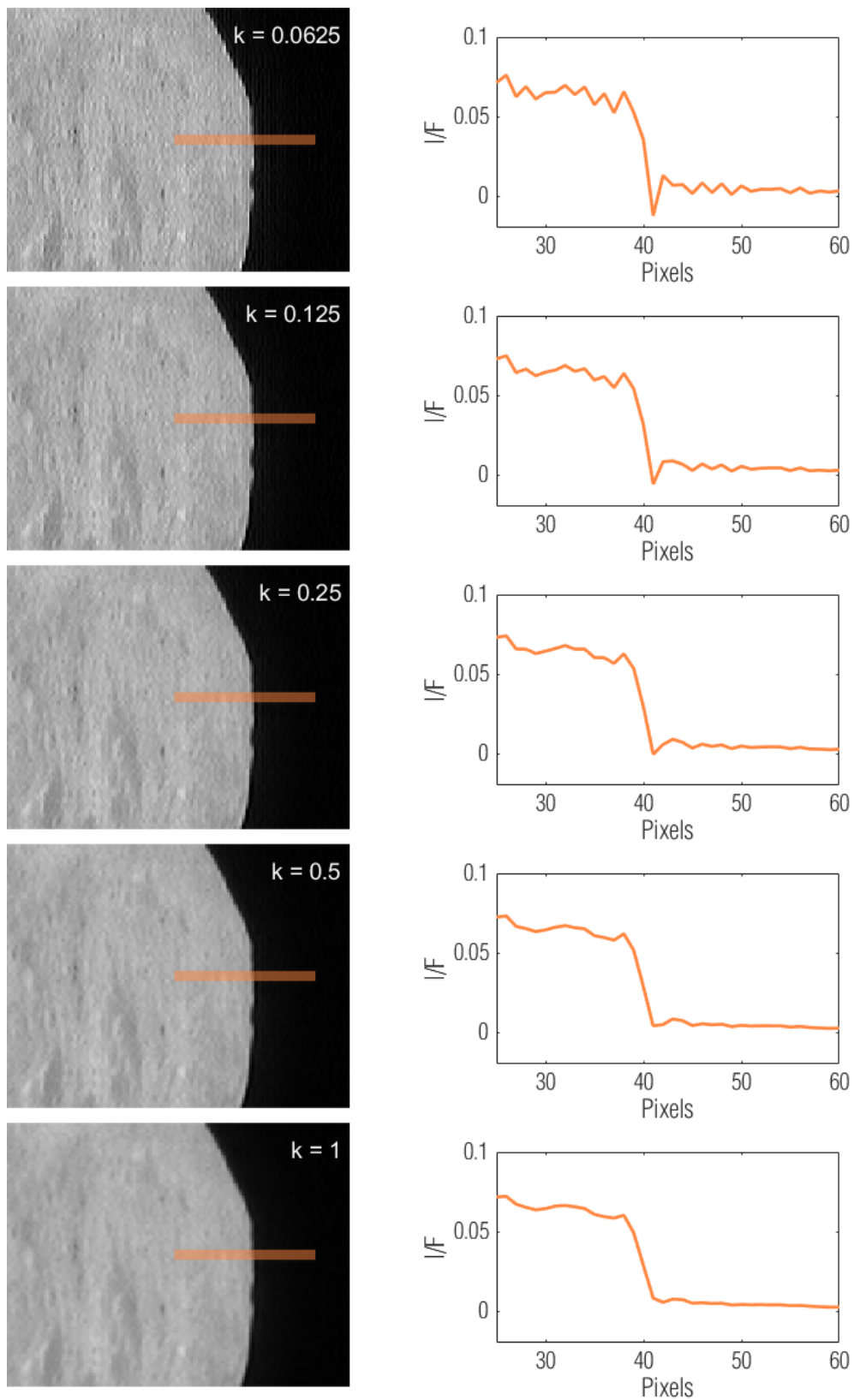
C_3	0.061	0.14	0.04	0.028	0.026	0.031	0.024	0.045
σ_{x1}	1.3	0.8	1.4	1.4	1.5	1.5	1	1.4
σ_{x2}	3.3	3	3	3	3.3	2.5	3	3.5
σ_{x3}	12	12	12	11	12	13	12	12
σ_{y1}	0.5	0.8	0.5	0.5	0.6	1	0.5	0.5
σ_{y2}	3	3	3	3	2.8	2.5	3	3
y_3	12	12	12	11	12	11	12	12
x_1	0.0037	0.0061	0.0048	0.0055	0.0036	0.0081	0.0085	0.0032
x_2	-0.55	-0.16	-0.58	-0.86	-0.83	-0.79	-0.5	-0.53
x_3	-0.34	-0.31	-0.34	-0.41	-0.38	-0.33	-0.84	-0.23
y_1	0.00088	-0.0044	0.00095	0.0034	-0.0055	0.0085	0.0028	0.002
y_2	-0.021	0.067	-0.067	-0.25	0.4	-0.33	-0.041	-0.18
y_3	-0.078	-0.19	-0.061	-0.085	0.095	-0.022	-0.0076	-0.17
k	2	6	0.4	0.25	0.2	0.3	3	0.4

304

305 To determine these parameters, we performed a series of qualitative analyses. These analyses uses
 306 images that span the range of scenes imaged by MSI (e.g., whole disk, limb, well illuminated, deeply
 307 shadowed).

308 We evaluate remediation images that include the limb (Figure 7(left)) by tracing profiles across the limb
 309 (Figure 7(right)), calculated as the median of several limb-crossing rows. Figure 7 illustrates the inherent
 310 trade-off: a sharper limb profile (lower k) indicates improved deblurring, but over-processing an image
 311 will lead to artifacts at the limb boundary. These artifacts manifest as ringing on either side of the
 312 discontinuity (most obvious in the top row), as well as a sharp peak and valley just before and after the
 313 limb. However, increasing the value of k to eliminate FFT artifacts (bottom row) results in poor
 314 deblurring performance and even that does not eliminate the peak before the limb. The valley after the
 315 limb is only eliminated because the limb has blurred enough to fill it in. Again, without a quantitative
 316 measure of accuracy, our parameters are guided by visual appearance and inherently qualitative.
 317 However, we make these choices informed by the needs of typical image data products (e.g.,
 318 monochromatic maps and color ratios).

319 Similarly, we evaluate images that don't include limb by tracing profiles across high contrast features.
 320 These include high albedo features (Fig X), deeply shadowed regions (Fig Y), and



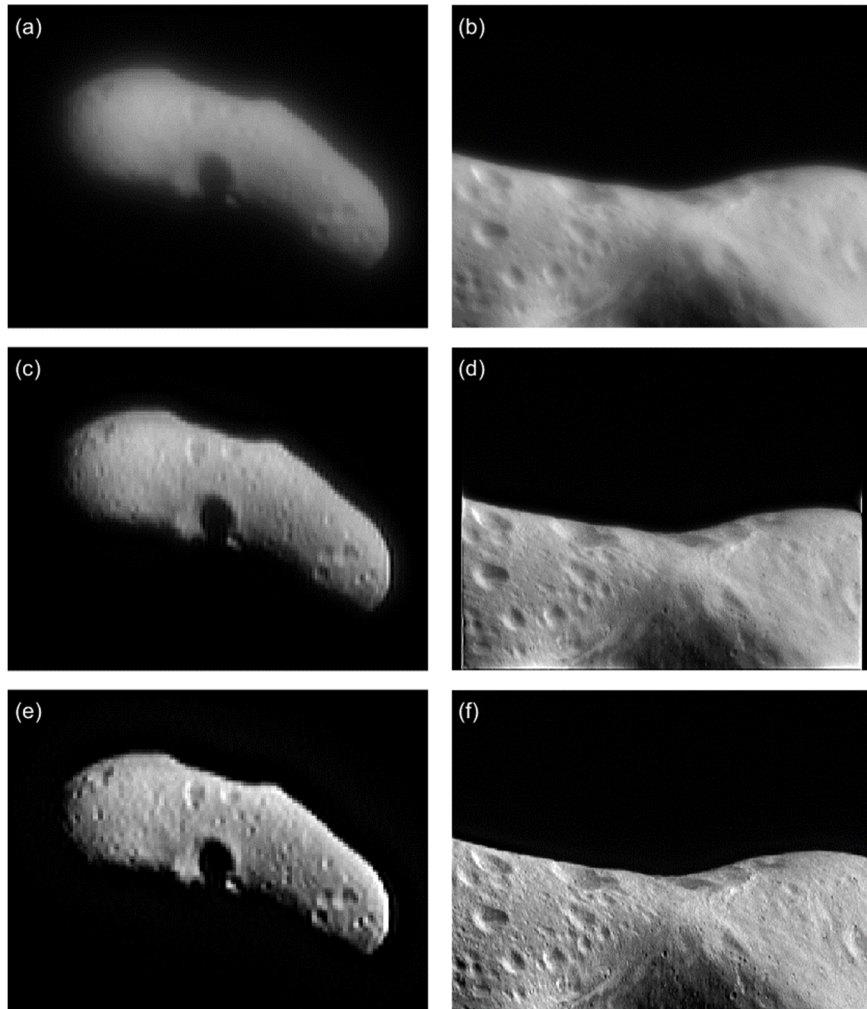
321

322 *Figure 7: Limb profiles of a remediated image (m0151057156) help determine the design of the PSF and magnitude of the noise*
 323 *term. Setting the noise term low produces a sharp limb profile, but setting the noise term high reduces ringing around the limb.*

324 **3 REMEDIATION QUALITY**

325 **3.1 Qualitative summary**

326 For all filters, the new remediation shows improvement over the preliminary version. We find that this is
327 primarily due to an alternative PSF model that allowed us to reduce the noise term. The asymmetry of
328 central Gaussian of the PSF model (σ_{x1} and σ_{y1} in Table 2) reduced the magnitude of FFT artifacts while
329 improving image quality (Section 2.7), but the trade between sharpness and noise remains (Section 2.8).
330 Though we evaluated the new remediation on a small subset of images (~100 out of the 100,000 image
331 database), the improvement was consistent. This included for whole disk images (Figure 8(a,c,e)), limb
332 images (Figure 8(b,d,f)), full field images (Figure 9), and images from every filter (Figure 10). The images
333 shown in these figures are given identical grayscale stretches to highlight the improvement qualitatively.
334 The depth of shadows (e.g., in craters) and reflectance on bright surfaces (e.g., crater rims) are
335 enhanced in the new remediation, producing a sharper appearance. Moreover, FFT artifacts, visible
336 extending ~10s of pixels from the edges of the images with the original remediation, are not present in
337 the new remediation.

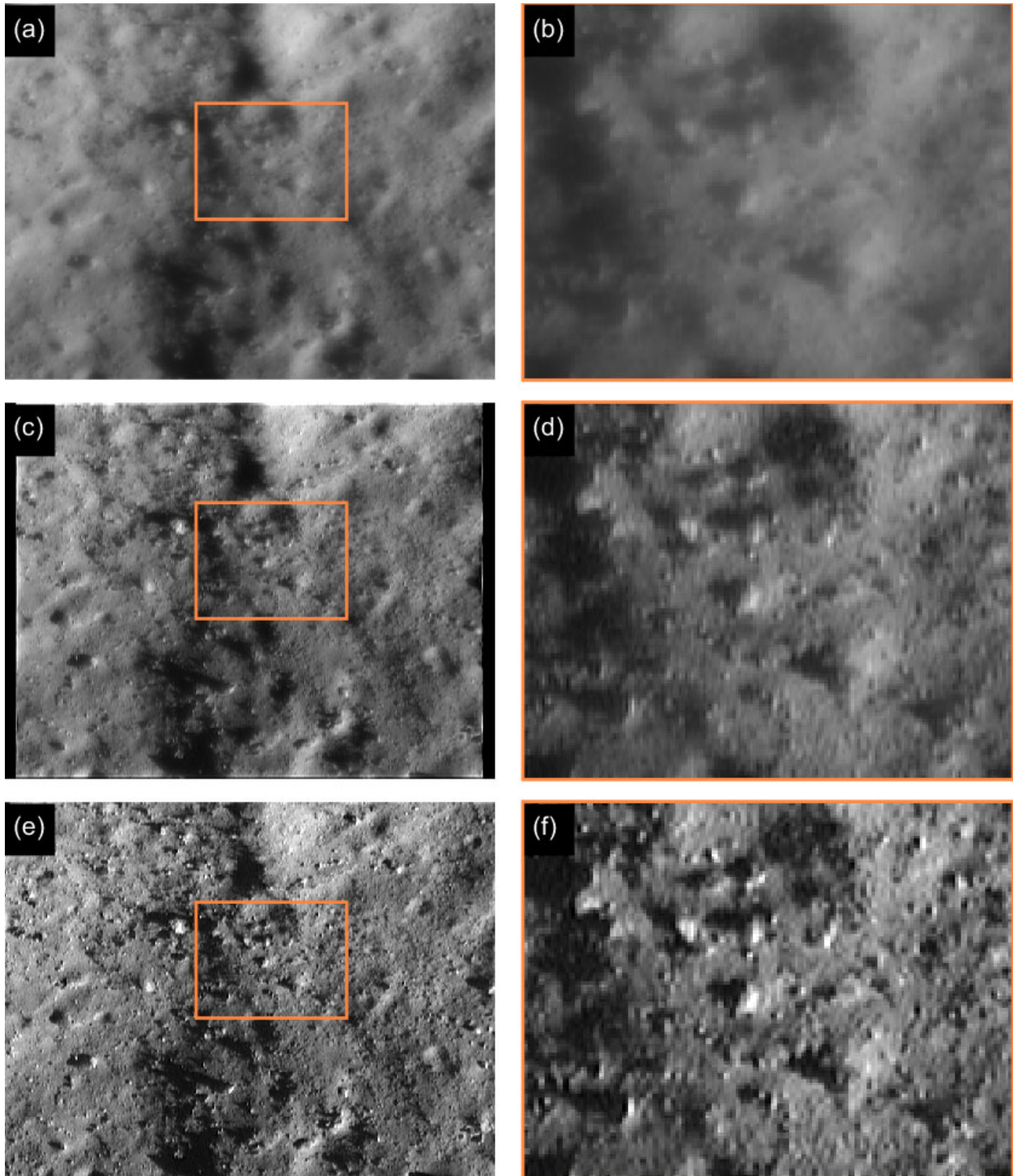


338

339 *Figure 8: Degraded images m0125680533 (a) and m0128004492 (b) acquired with filter 4 (950 nm) improved significantly with*
340 *the preliminary remediation (c,d; Li et al. 2002), but asymmetric PSF design allowed for further improvement in this work (e,f).*

341 Images on the left are cropped to a 165 x 127 window around the asteroid.
342 An identical greyscale stretch is applied to each
version of each image (different stretches for the two columns).

343

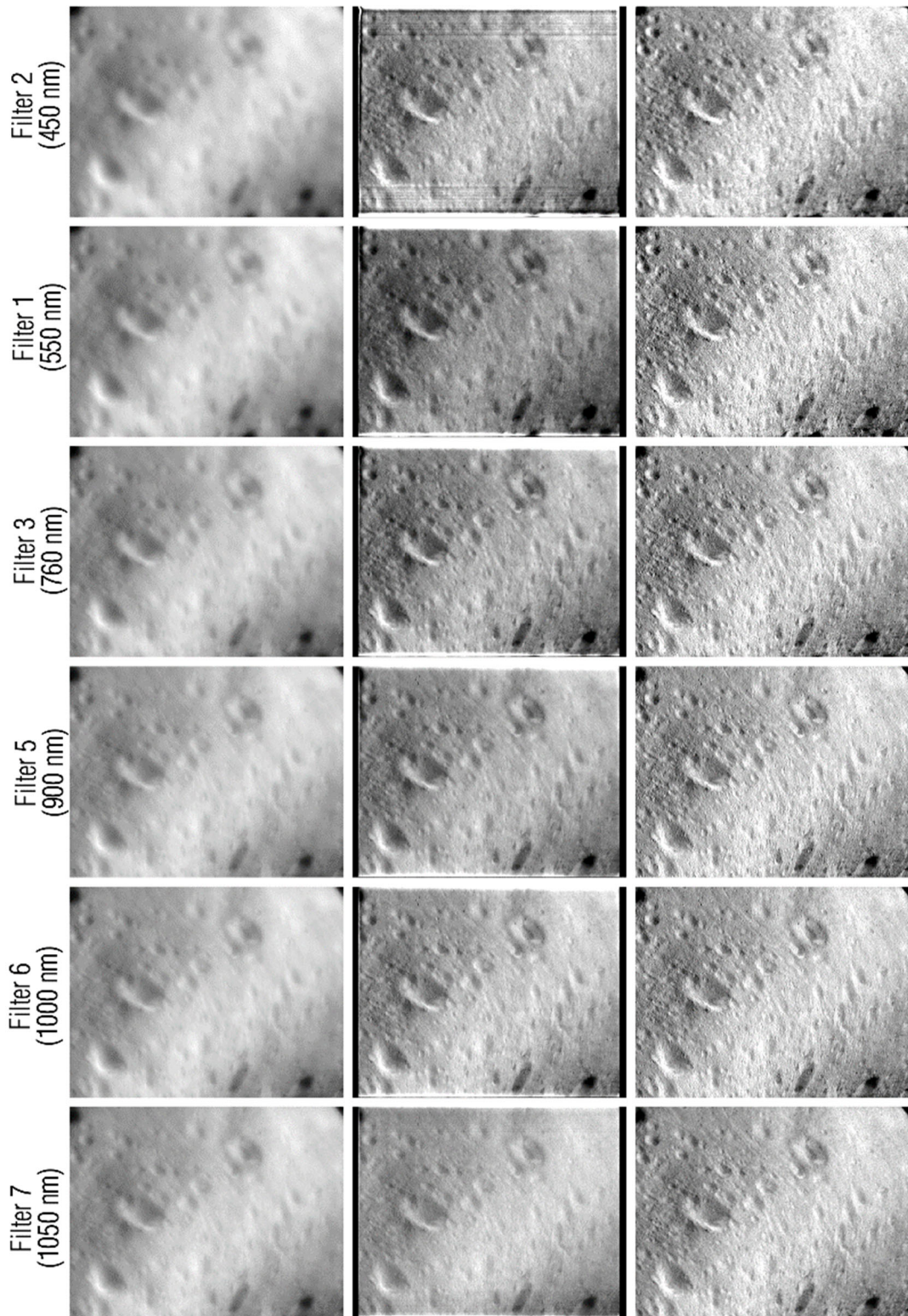


344

345 Figure 9: Additional example of degraded image m0153333885 (a,b) acquired with filter 4 (950 nm), its original remediation
346 (c,d), and its new remediation (e,f). The right column (b,d,f) is a zoomed in region. All images have an identical grayscale stretch.

347

348



349

350 *Figure 10: Degraded images (left), original remediation (middle), and new remediation (right) for additional filters. Image*
351 *numbers are m0150981856, m0150981854, m0150981858, m0150981862, m0150981864, m0150981866 for filters 2, 1, 3, 5, 6,*
352 *and 7, respectively. All three images from each filter have the same grayscale stretch.*

353 3.2 Filters 2 and 7

354 As shown in Figure 10, all filters show improvement over the original remediation, but filters 2 (450 nm)
355 and 7 (1050 nm) remain the least well corrected. As described in Li et al. (2002), the contamination had
356 the largest impact on the extreme wavelength filters. In that original remediation, they were unable to
357 correct these filters as well, and many had extreme FFT artifacts (Figure 10). As such, the PSF model we
358 designed for these filters (Table 2), are noticeably different from the rest. Their central Gaussians are
359 narrower with a smaller peak (relative to the other two Gaussian components). Moreover, the SNR of
360 images acquired with these filters is uniformly lower than the other filters. The camera is less sensitive
361 in filter 2 (450 nm) due to the quantum efficiency of the detector and transmission of the optics
362 (Hawkins et al., 1997), necessitating exposure times 2.5-5X longer than the middle wavelengths.
363 Exposure times are even longer (10-20X) for filter 7 (1050 nm), due to lower detector quantum
364 efficiency at longer wavelengths (Hawkins et al., 1997). Using an unrealistically low noise term
365 introduces speckle FFT artifacts (i.e., noise in the original image is amplified in the deconvolution
366 process). As a result, we set the noise terms much higher in filters 2 and 7. This sacrifices some image
367 quality, but avoids extreme FFT noise.

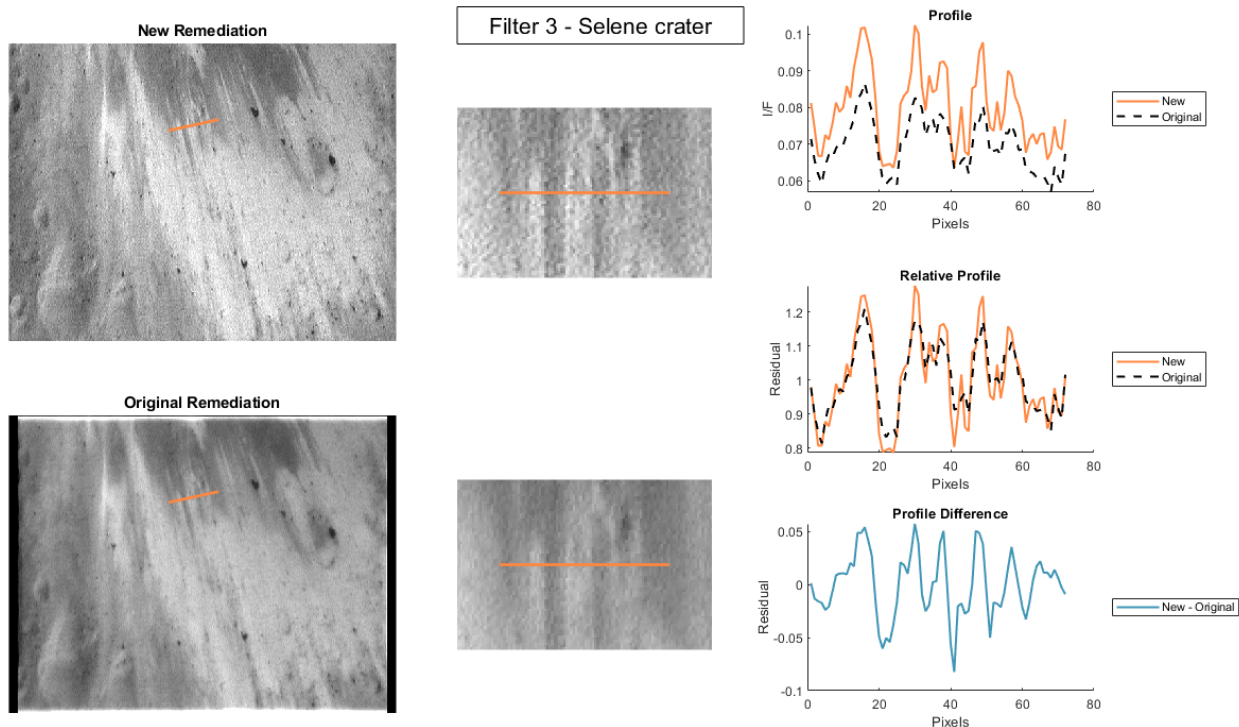
368 3.3 Quantitative analysis

369 We were not able to develop a thorough quantitative analysis of the improved remediation. As with
370 identifying an ‘ideal’ noise factor (Section 2.8), such an analysis requires a robust quantitative quality
371 metric. Every metric we investigated to design the deblurring parameters was sensitive to both image
372 sharpness and high frequency noise. However, high-contrast surface features provide an opportunity to
373 quantitatively evaluate the new remediation for particular geological units. Moreover, these are exactly
374 the types of surface features that an improved remediation will allow further study of.

375 The geological features we analyzed included bright streaks (Selene crater at 760 nm; Figure 11), dark
376 deposits (Psyche crater at 450 nm; Figure 12) and streaks (Psyche crater at 1000 nm; Figure 13), crater
377 walls (Avtandil crater at 550 and Selene crater at 900 nm; Figure 14 and Figure 15), boulders (950 nm;
378 Figure 16), and the asteroid limb (1050 nm; Figure 17). The analysis in these images traces a profile
379 perpendicular to the contrast boundary created by the feature. We rotated the images such that the
380 profiles were horizontal (i.e., along a row) and calculated the median of 5 rows around and including the
381 profile line. The median partially smoothed the pixel-to-pixel variation that is present in the images,
382 though an obvious residual variation remains in many examples and is discussed further below. The
383 figures show an image corrected with the new and original remediations. The left column shows the full
384 images; the middle column crops to the region of the profile. All images are given the same grayscale
385 stretch. The absolute profiles (in units of I/F) are plotted in the top-right. Because the new remediation
386 also includes new radiometric correction (Section 4), the mean I/F of an image can be different when
387 compared with the original remediation. To remove this from the comparison, we calculate a linear fit to
388 each profile and divide it into the profile. This effectively removes the absolute I/F calibration and any
389 local reflectance slope. The result is shown in the middle-right plot for both methods and demonstrates
390 how well the remediation methods resolve reflectance changes. Finally, the difference between these
391 relative profiles is plotted in the bottom-right to provide a quantitative estimate of the remediation
392 quality.

393 These examples provide a number of insights with respect to the quality of the new remediation. High
 394 contrast features are, in general, better resolved with the new remediation. That is, the contrast change
 395 'on' and 'off' the feature is greater. This is illustrated by Figure 14, which traces a profile across the
 396 bright wall of Avtandil crater. The reflectance of the bright wall is 50% brighter than the surrounding
 397 terrain in the original remediation, but 65% brighter in the new remediation. Other examples of higher
 398 frequency features (such as bright and dark streaks), show similar behavior, but are muddled by high
 399 frequency noise. For example, the contrast variation between bright streaks in Selene crater (Figure 11)
 400 is amplified (i.e., the peaks and valleys are further from the reflectance average) in the new remediation,
 401 but noise in the image is similarly amplified. So while the bright streaks have ~5% higher contrast in the
 402 new remediation, background noise has ~2% higher contrast. This background noise is often visible in
 403 regions without measurable signal (such as deep shadows or off-limb), where scene-independent noise
 404 (e.g., shot noise, read noise, uncorrected dark current) is amplified. This reinforces the fundamental
 405 trade-off between sharpness and noise (Section 2.8). Often, as in the 450 nm image of dark deposits on
 406 Psyche crater (Figure 12), the noise is present in both methods, but the noise is better 'resolved' with
 407 the new remediation. Nonetheless, high contrast features, such as the transition between a boulder's
 408 shadow and its sunlit side (Figure 16), show tens of percent increase in contrast with the new
 409 remediation. Limb profiles, which were partially used to design the new PSF and noise terms, show a
 410 similar level of improvement (Figure 17). These examples are a very small fraction of the large MSI Eros
 411 dataset and they have been chosen to highlight the improvement made possible by the new
 412 remediation. Many images have minimal improvement over the original remediation, though we have
 413 not found any that show degradation. Nonetheless, because the new images have generally improved
 414 sharpness, they often have generally increased noise.

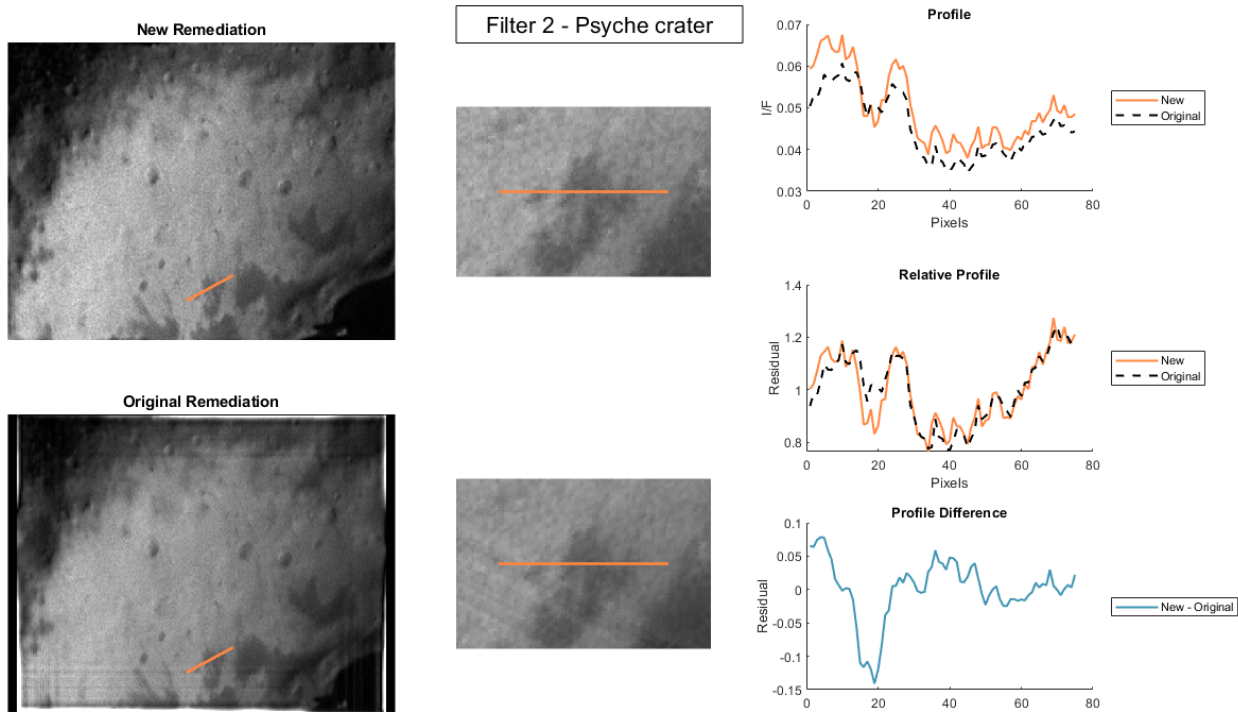
415



416

417 *Figure 11: Profile analysis of bright streaks in Selene crater, imaged at 760 nm (m0155816391).*

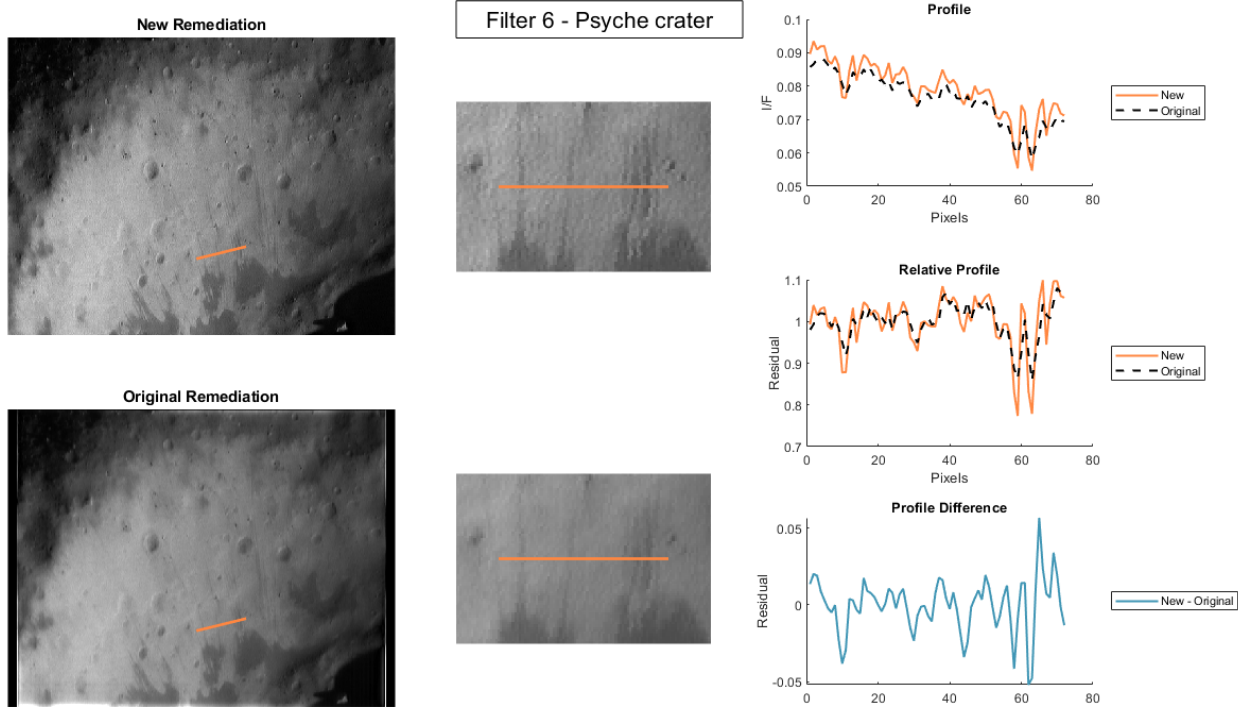
418



419

420

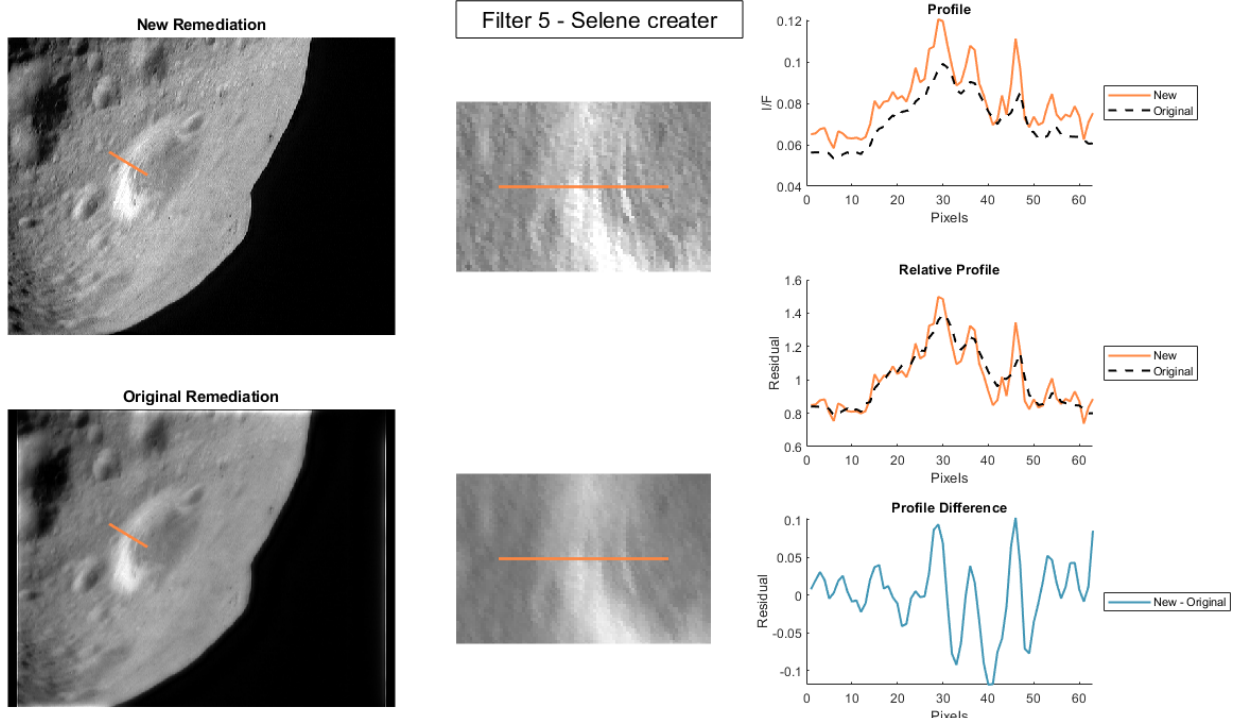
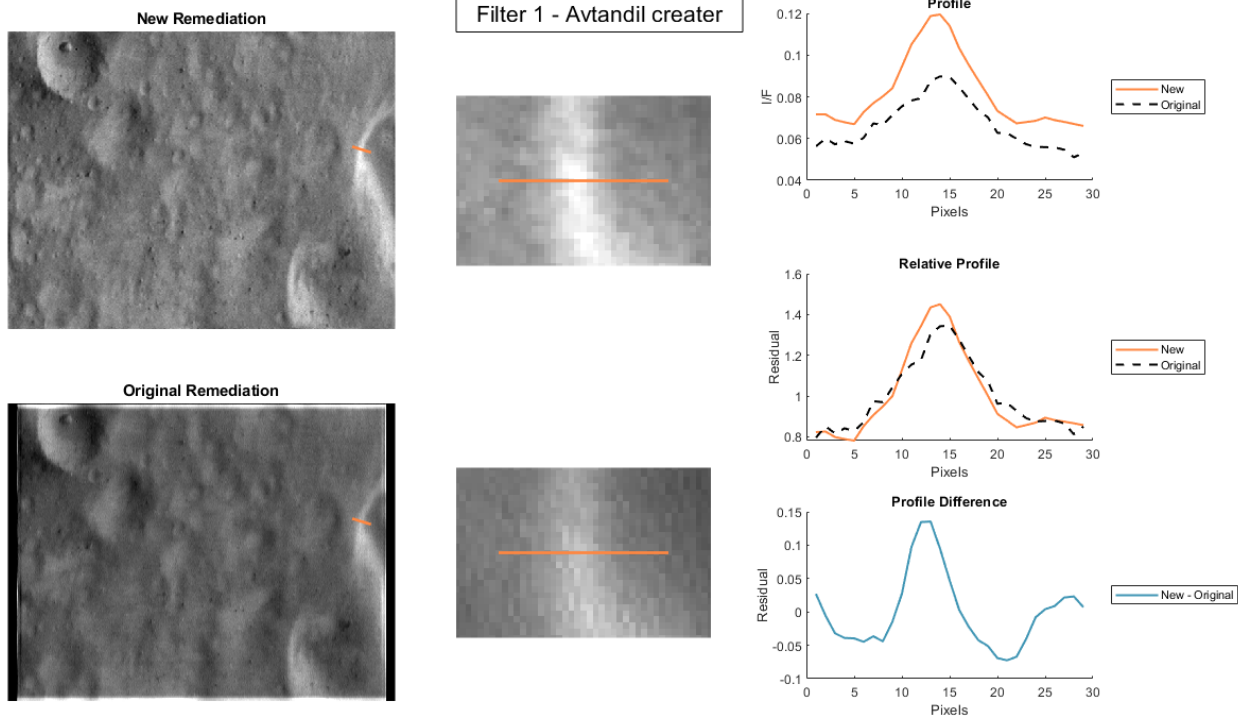
Figure 12: Profile analysis of dark deposits in Psyche crater, imaged at 450 nm (m0141515386).

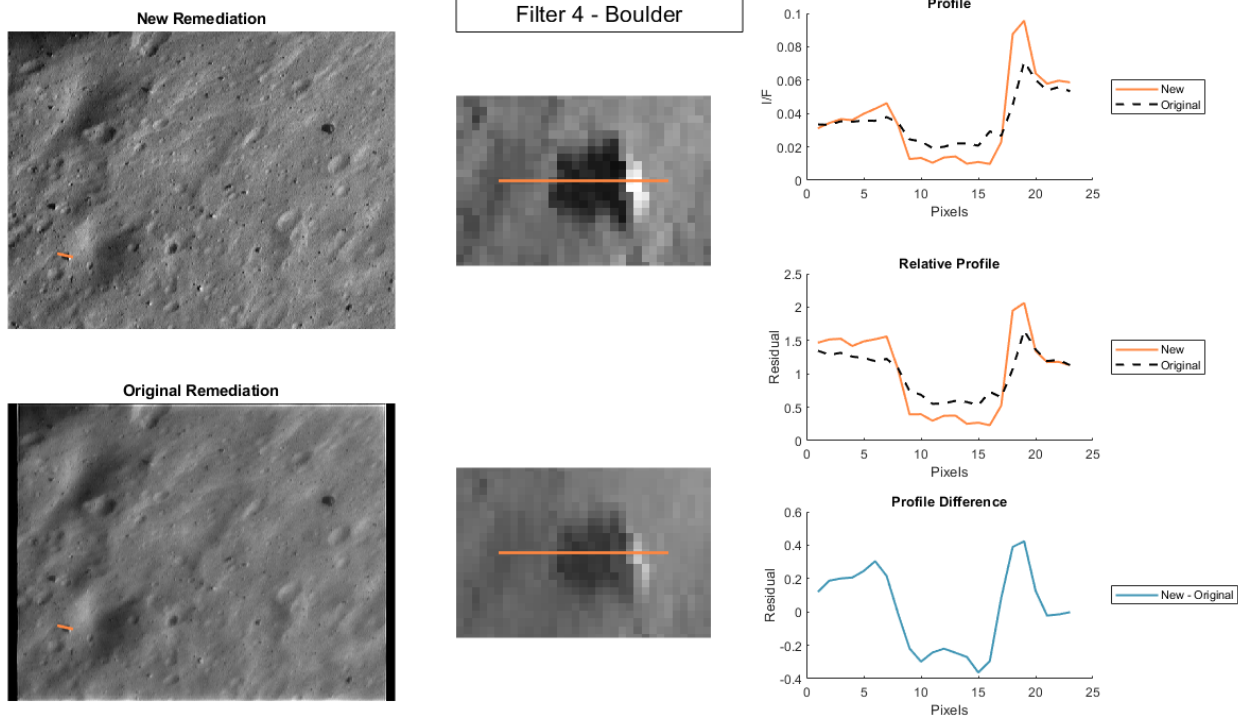


421

422

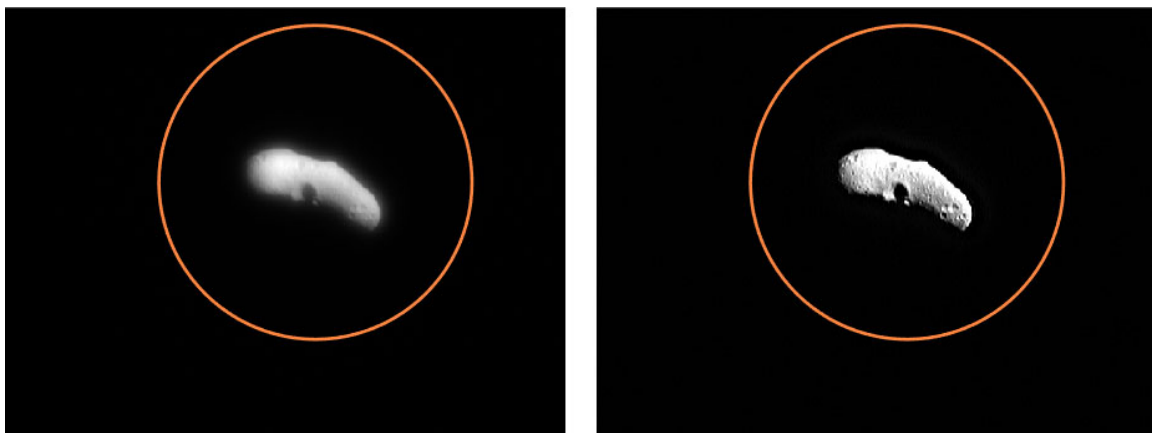
Figure 13: Profile analysis of dark streaks in Psyche crater, imaged at 1000 nm (m0141515392).





434 **4 RADIOMETRIC CORRECTION**

435 Blur remediation shifts a significant portion of the optical energy between pixels. Consequently, the
436 radiometric (radiance or I/F) values are incorrect without further correction. We follow the strategy
437 outlined in (Li et al., 2002) to apply an absolute radiometric calibration, wherein we assume that energy
438 is conserved in the remediation process. That is, all energy measured in the original (degraded) images
439 exists in the final (remediated) images, it has only been shifted between pixels. Therefore, we forced the
440 sum of the energy in the region surrounding the asteroid in a remediated image to match that in its
441 corresponding degraded image. This is most accurate when we perform it on a whole disk image (Figure
442 18), where all measured energy is captured within the MSI field of view.



443

444 *Figure 18: Degraded whole disk images (left) provide a radiometric normalization for recovered images (right) by summing the*
445 *energy surrounding the asteroid (indicated by orange circle). The example shown was acquired with filter 4 (m0125680533).*

446 Because the degraded images have signal past the asteroid limb (e.g., the glow and halo discussed in
447 Section 2.7), we summed the energy well past the limb so that any blurred energy was captured in the
448 sum. We tested summing the entire image versus summing a 150 pixel radius circle around Eros and
449 found the differences to be <0.02% for all filters. We repeated this calculation for whole disk images
450 acquired by all eight filters on 11 February and 12 February, 2000 (312 images total) and calculated the
451 median radiometric correction for each filter. The number of images, per filter, and median radiometric
452 correction are listed in Table 3. These values were calculated for and applied to the data described in
453 this paper. Unfortunately, if a user applies their own remediation with the published code (Section 5),
454 using customized PSF and noise term values, the radiometric correction parameters in Table 3 will be
455 theoretically invalid. Though small changes in the remediation parameters will have a small effect on the
456 radiometric correction, users should nonetheless take caution and consider calculating new radiometric
457 correction factors by reproducing the radiometric analysis described here for differently deblurred data.

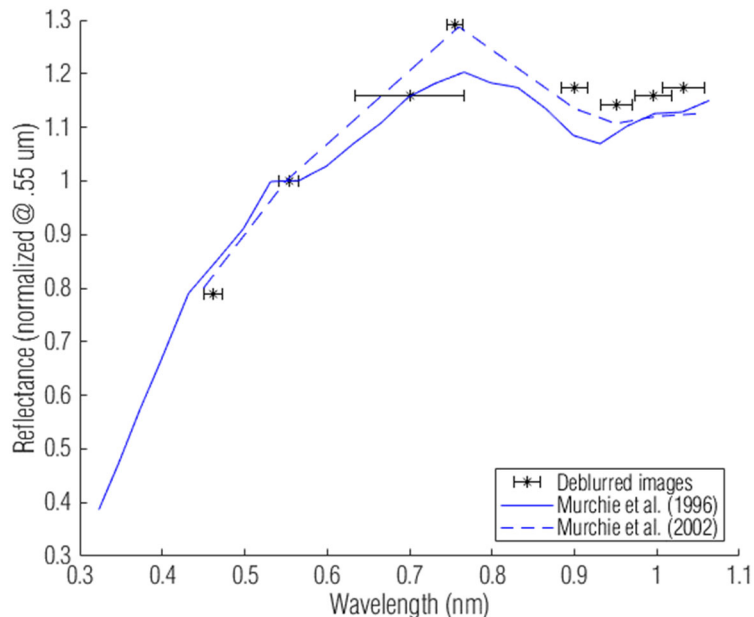
458 In any image where energy (i.e. Eros) is at the edge of the field of view, some of it will have been blurred
459 off the detector. That energy is lost in the measurement and cannot be recovered. However, the surface
460 that is just outside the field of view will partially blur onto the detector. To first order, these effects
461 cancel each other out and do not require additional radiometric correction. This is not valid in edge
462 cases where an extremely bright or dark scene is present just outside the field of view (e.g., an image
463 where the asteroid limb is exactly at the edge of the image). However, we assume that these cases are
464 sufficiently rare that we take no additional steps to accommodate them.

465 *Table 3: Radiometric corrections for each filter*

Filter (wavelength, nm)	Number of images	Radiometric correction
1 (550)	43	32.49
2 (450)	43	69.66
3 (760)	43	21.03
4 (950)	42	14.54
5 (900)	43	15.77
6 (1000)	43	18.26
7 (1050)	42	17.61
0 (pan)	12	24.68

466

467 We verified the relative (filter-to-filter) radiometric calibration by calculating a spectrum of Eros using
 468 the same whole disk images and comparing to published spectra (Murchie et al., 2002a; Murchie, 1996).
 469 We normalized the data at 550 nm to eliminate the absolute radiometric component. The difference
 470 between our calibration and the published spectra is within the MSI radiometric uncertainty (5%)
 471 determined by Murchie et al. (2002b, 1999) and within the difference between the published spectra.



472

473 *Figure 19: Comparison of relative radiometric calibration of the new remediation (black asterisks) with published spectra of Eros*
 474 *(blue lines). Horizontal error bars indicate the width of each MSI filter.*

475 **5 CODE AVAILABILITY AND CONCLUSIONS**

476 We have updated the blur remediation method first published by Li et al. (2002) to utilize an asymmetric
 477 model of the MSI optics after hydrazine contamination. This new model, which we functionally define as
 478 the sum of three Gaussians, allows for recovery of additional spatial content from the degraded images.
 479 We demonstrated this improvement both visually and with the contrast examples given in Section 3.3.

480 However, an objective measure of ‘improvement’ is illusive and depends strongly on the desired
481 application of the images.

482 In addition, we add tapered symmetric padding to the FFT-based deconvolution to eliminate the FFT
483 artifacts that were present along the edges of images with the original remediation. The changes
484 increase the usable pixels in the images by 21-39%.

485 We have applied the new correction to all MSI images acquired during 2000 and 2001 that are currently
486 available in the PDS SBN (<https://sbn.psi.edu/pds/resource/near/msiinst.html>). We will archive the
487 newly corrected images at the PDS Imaging Node. As noted in Section 2.3, the images are not scaled
488 back to their native pixel format (as the raw and original remediation data are); they are left at the
489 physically meaningful aspect ratio (412×537).

490 As demonstrated in the variety of examples provided in this manuscript, the choice of PSF and noise
491 terms is inherently arbitrary and sensitive. Although the remediation we present here (and archived
492 with the PDS) was performed with terms that we believed produced the best trade-off between
493 sharpness and noise, these choices may not apply to all images or applications. For instance, color
494 analyses are typically very sensitive to pixel-level noise (DellaGiustina et al., 2020; Murchie et al., 2002a;
495 Tatsumi et al., 2021), which is amplified in color ratios. As such, a color analysis may wish to apply a
496 different correction level to the images.

497 For example, we have found, in color analyses that are beyond the scope of this manuscript, that color
498 ratios (using overlapping images from different filters) require noise removal techniques (e.g., low pass
499 filtering and Gaussian blurring) to maintain spatially coherent structure. This filtering essentially
500 removes much of the sharpness recovered in this work. Nonetheless, our analyses found that using the
501 newly remediated images was an improvement because it allowed for underlying, single-filter basemaps
502 to have improved contrast (Section 3.3) and updated radiometric correction (Section 4).

503 To provide the most utility from this remediation, we are also publishing the code used to apply the
504 remediation. That code is seeded with the PSF and noise term values given in Table 2, but those values
505 can be adjusted as necessary. The code is written in MATLAB and is available at
506 <https://NASAGITHUBURL>.

507 6 ACKNOWLEDGMENTS

508 This work comes two decades after the end of the NEAR mission, the success of which was due to a
509 large number of individuals in the operational and scientific teams. Their efforts provided the
510 exceptional dataset we attempted to improve. The work here builds directly off the original remediation
511 developed by the MSI team, specifically Han Li and Mark Robinson, during NEAR operations. We also
512 thank Mark Robinson for providing code, data, and insight for their original remediation work and Beth
513 Clark for reviewing the manuscript.

514 The image data in this work are archived in the Planetary Data System Small Bodies Node at
515 <https://sbn.psi.edu/pds/resource/near/msiinst.html>. This work was supported by NASA under Contract
516 NNH18ZDA001N-PDART issued through the Planetary Data, Archiving, Restoration, and Tools program.

517 7 REFERENCES

- 518 Acton, C., Bachman, N., Semenov, B., Wright, E., 2018. A look towards the future in the handling of
519 space science mission geometry. *P&SS* 150, 9–12. <https://doi.org/10.1016/j.pss.2017.02.013>
- 520 Buczkowski, D.L., Barnouin-Jha, O.S., Prockter, L.M., 2008. 433 Eros lineaments: Global mapping and
521 analysis. *Icarus* 193, 39–52. <https://doi.org/10.1016/j.icarus.2007.06.028>
- 522 Bussey, D.B.J., Robinson, M.S., Edwards, K., Thomas, P.C., Joseph, J., Murchie, S., Veverka, J., Harch, A.P.,
523 2002. 433 Eros Global Basemap from NEAR Shoemaker MSI Images. *Icarus* 155, 38–50.
524 <https://doi.org/10.1006/icar.2001.6771>
- 525 Cheng, A.F., Izenberg, N., Chapman, C.R., Zuber, M.T., 2002. Ponded deposits on asteroid 433 Eros.
526 *Meteoritics and Planetary Science* 37, 1095–1105. <https://doi.org/10.1111/j.1945-5100.2002.tb00880.x>
- 528 Cheng, A.F., Santo, A.G., Heeres, K.J., Landshof, J.A., Farquhar, R.W., Gold, R.E., Lee, S.C., 1997. Near-
529 Earth Asteroid Rendezvous: Mission overview. *JGRE* 102, 23695–23708.
530 <https://doi.org/10.1029/96JE03364>
- 531 DellaGiustina, D.N., Burke, K.N., Walsh, K.J., Smith, P.H., Golish, D.R., Bierhaus, E.B., Ballouz, R.-L.,
532 Becker, T.L., Campins, H., Tatsumi, E., Yumoto, K., Sugita, S., Deshapriya, J.D.P., Cloutis, E.A., Clark,
533 B.E., Hendrix, A.R., Sen, A., Al Asad, M.M., Daly, M.G., Applin, D.M., Avdellidou, C., Barucci, M.A.,
534 Becker, K.J., Bennett, C.A., Bottke, W.F., Brodbeck, J.I., Connolly, H.C., Delbo, M., de Leon, J.,
535 Drouet d'Aubigny, C.Y., Edmundson, K.L., Fornasier, S., Hamilton, V.E., Hasselmann, P.H.,
536 Hergenrother, C.W., Howell, E.S., Jawin, E.R., Kaplan, H.H., Le Corre, L., Lim, L.F., Li, J.Y., Michel, P.,
537 Molaro, J.L., Nolan, M.C., Nolau, J., Pajola, M., Parkinson, A., Popescu, M., Porter, N.A., Rizk, B.,
538 Rizos, J.L., Ryan, A.J., Rozitis, B., Shultz, N.K., Simon, A.A., Trang, D., Van Auken, R.B., Wolner, C.W.
539 V., Lauretta, D.S., 2020. Variations in color and reflectance on the surface of asteroid (101955)
540 Bennu. *Science* 370, eabc3660. <https://doi.org/10.1126/science.abc3660>
- 541 Dhawan, A.P., Rangayyan, R.M., Gordon, R., 1985. Image restoration by Wiener deconvolution in
542 limited-view computed tomography. *Applied Optics* 24, 4013.
543 <https://doi.org/10.1364/AO.24.004013>
- 544 Dombard, A.J., Barnouin, O.S., Prockter, L.M., Thomas, P.C., 2010. Boulders and ponds on the Asteroid
545 433 Eros. *Icarus* 210, 713–721. <https://doi.org/10.1016/j.icarus.2010.07.006>
- 546 Golish, D.R., Drouet d'Aubigny, C., Rizk, B., DellaGiustina, D.N., Smith, P.H., Becker, K., Shultz, N., Stone,
547 T., Barker, M.K., Mazarico, E., Tatsumi, E., Gaskell, R.W., Harrison, L., Merrill, C., Fellows, C.,
548 Williams, B., O'Dougherty, S., Whiteley, M., Hancock, J., Clark, B.E., Hergenrother, C.W., Lauretta,
549 D.S., 2020. Ground and In-Flight Calibration of the OSIRIS-REx Camera Suite. *SSRv* 216, 12.
550 <https://doi.org/10.1007/s11214-019-0626-6>
- 551 Hawkins, S.E., 1998. The NEAR multispectral imager. Johns Hopkins APL Technical Digest (Applied
552 Physics Laboratory) 19, 107–114.
- 553 Hawkins, S.E., Darlington, E.H., Murchie, S.L., Peacock, K., Harris, T.J., Hersman, C.B., Elko, M.J.,
554 Prendergast, D.T., Ballard, B.W., Gold, R.E., Veverka, J., Robinson, M.S., 1997. Multi-Spectral Imager
555 on the Near Earth Asteroid Rendezvous mission. *SSRv* 82, 31–100.
556 <https://doi.org/10.1023/A:1005099211710>

- 557 Izenberg, N.R., Murchie, S.L., Bell, J.F., McFadden, L.A., Wellnitz, D.D., Clark, B.E., Gaffey, M.J., 2003.
558 Spectral properties and geologic processes on Eros from combined NEAR NIS and MSI data sets.
559 Meteoritics and Planetary Science 38, 1053–1077. <https://doi.org/10.1111/j.1945-5100.2003.tb00298.x>
- 561 Janesick, J.R., 2001. Scientific Charge-Coupled Devices. SPIE, 1000 20th Street, Bellingham, WA 98227-
562 0010 USA. <https://doi.org/10.1117/3.374903>
- 563 Li, H., Robinson, M.S., Murchie, S., 2002. Preliminary Remediation of Scattered Light in NEAR MSI
564 Images. Icarus 155, 244–252. <https://doi.org/10.1006/icar.2001.6745>
- 565 Li, J., A'Hearn, M.F., McFadden, L.A., 2004. Photometric analysis of Eros from NEAR data. Icarus 172,
566 415–431. <https://doi.org/10.1016/j.icarus.2004.07.024>
- 567 Murchie, S., Robinson, M., Clark, B., Li, H., Thomas, P., Joseph, J., Bussey, B., Domingue, D., Veverka, J.,
568 Izenberg, N., Chapman, C., 2002a. Color Variations on Eros from NEAR Multispectral Imaging.
569 Icarus 155, 145–168. <https://doi.org/10.1006/icar.2001.6756>
- 570 Murchie, S., Robinson, M., Domingue, D., Li, H., Prockter, L., Hawkins, S.E., Owen, W., Clark, B., Izenberg,
571 N., 2002b. Inflight Calibration of the NEAR Multispectral Imager II. Results from Eros Approach and
572 Orbit. Icarus 155, 229–243. <https://doi.org/10.1006/icar.2001.6746>
- 573 Murchie, S., Robinson, M., Hawkins, S.E., Harch, A., Helfenstein, P., Thomas, P., Peacock, K., Owen, W.,
574 Heyler, G., Murphy, P., Darlington, E.H., Keeney, A., Gold, R., Clark, B., Izenberg, N., Bell, J.F.,
575 Merline, W., Veverka, J., 1999. Inflight Calibration of the NEAR Multispectral Imager. Icarus 140,
576 66–91. <https://doi.org/10.1006/icar.1999.6118>
- 577 Murchie, S.L., 1996. Spectral properties and rotational spectral heterogeneity of 433 Eros. JGRE 101,
578 2201–2214. <https://doi.org/10.1029/95JE03438>
- 579 Riner, M.A., Robinson, M.S., Eckart, J.M., Desch, S.J., 2008. Global survey of color variations on 433 Eros:
580 Implications for regolith processes and asteroid environments. Icarus 198, 67–76.
581 <https://doi.org/10.1016/j.icarus.2008.07.007>
- 582 Robinson, M.S., Thomas, P.C., Veverka, J., Murchie, S.L., Wilcox, B.B., 2002. Invited Review The geology
583 of 433 Eros, Meteoritics & Planetary Science.
- 584 Sierks, H., Keller, H.U., Jaumann, R., Michalik, H., Behnke, T., Bubenhausen, F., Büttner, I., Carsenty, U.,
585 Christensen, U., Enge, R., Fiethe, B., Gutiérrez Marqués, P., Hartwig, H., Krüger, H., Kühne, W.,
586 Maue, T., Mottola, S., Nathues, A., Reiche, K.-U., Richards, M.L., Roatsch, T., Schröder, S.E.,
587 Szemerey, I., Tschentscher, M., 2011. The Dawn Framing Camera. SSRv 163, 263–327.
588 <https://doi.org/10.1007/s11214-011-9745-4>
- 589 Tatsumi, E., Sakatani, N., Riu, L., Matsuoka, M., Honda, R., Morota, T., Kameda, S., Nakamura, T.,
590 Zolensky, M., Brunetto, R., Hiroi, T., Sasaki, S., Watanabe, S., Tanaka, S., Takita, J., Pilorget, C., de
591 León, J., Popescu, M., Rizos, J.L., Licandro, J., Palomba, E., Domingue, D., Vilas, F., Campins, H., Cho,
592 Y., Yoshioka, K., Sawada, H., Yokota, Y., Hayakawa, M., Yamada, M., Kouyama, T., Suzuki, H.,
593 Honda, C., Ogawa, K., Kitazato, K., Hirata, Naru, Hirata, Naoyuki, Tsuda, Y., Yoshikawa, M., Saiki, T.,
594 Terui, F., Nakazawa, S., Takei, Y., Takeuchi, H., Yamamoto, Y., Okada, T., Shimaki, Y., Shirai, K.,
595 Sugita, S., 2021. Spectrally blue hydrated parent body of asteroid (162173) Ryugu. NatCo 12.
596 <https://doi.org/10.1038/s41467-021-26071-8>
- 597 Thomas, P.C., Joseph, J., Carcich, B., Veverka, J., Clark, B.E., Bell, J.F., Byrd, A.W., Chomko, R., Robinson,

598 M., Murchie, S., Prockter, L., Cheng, A., Izenberg, N., Malin, M., Chapman, C., McFadden, L.A., Kirk,
599 R., Gaffey, M., Lucey, P.G., 2002. Eros: Shape, topography, and slope processes. *Icarus* 155, 18–37.
600 <https://doi.org/10.1006/icar.2001.6755>

601 Thomas, P.C., Robinson, M.S., 2005. Seismic resurfacing by a single impact on the asteroid 433 Eros.
602 *Nature* 436, 366–369. <https://doi.org/10.1038/nature03855>

603 Veverka, J., Robinson, M., Thomas, P., Murchie, S., Bell, J.F., Izenberg, N., Chapman, C., Harch, A., Bell,
604 M., Carcich, B., Cheng, A., Clark, B., Domingue, D., Dunham, D., Farquhar, R., Gaffey, M.J., Hawkins,
605 E., Joseph, J., Kirk, R., Li, H., Lucey, P., Malin, M., Martin, P., McFadden, L., Merline, W.J., Miller,
606 J.K., Owen, J., Peterson, C., Prockter, L., Warren, J., Wellnitz, D., Williams, B.G., Yeomans, D.K.,
607 2000. NEAR at Eros: Imaging and spectral results. *Science* 289, 2088–2097.
608 <https://doi.org/10.1126/science.289.5487.2088>

609 Zuber, M.T., Smith, D.E., Cheng, A.F., Garvin, J.B., Aharonson, O., Cole, T.D., Dunn, P.J., Guo, Y., Lemoine,
610 F.G., Neumann, G.A., Rowlands, D.D., Torrence, M.H., 2000. The shape of 433 Eros from the NEAR-
611 Shoemaker Laser Rangefinder. *Science* 289, 2097–2101.
612 <https://doi.org/10.1126/science.289.5487.2097>

613